Reversible Phase Transition for Durable Formamidinium-Dominated Perovskite Photovoltaics

Document license:
TAVERNE

DOI:
10.1002/adma.202204458

Document status and date:
Published: 28/09/2022

Document Version:
Publisher's PDF, also known as Version of Record (includes final page, issue and volume numbers)

Please check the document version of this publication:

• A submitted manuscript is the version of the article upon submission and before peer-review. There can be important differences between the submitted version and the official published version of record. People interested in the research are advised to contact the author for the final version of the publication, or visit the DOI to the publisher's website.
• The final author version and the galley proof are versions of the publication after peer review.
• The final published version features the final layout of the paper including the volume, issue and page numbers.

Link to publication

Reversible Phase Transition for Durable Formamidinium-Dominated Perovskite Photovoltaics

Huifen Liu, Nengxu Li, Zehua Chen, Shuxia Tao, Chunlei Li, Lang Jiang, Xiuxiu Niu, Qi Chen, Feng Wang, Yu Zhang, Zijian Huang, Tinglu Song, and Huanping Zhou*

Phase instability is one of the major obstacles to the wide application of forma-midinium (FA)-dominated perovskite solar cells (PSCs). An in-depth investigation on relevant phase transitions is urgently needed to explore more effective phase-stabilization strategies. Herein, the reversible phase-transition process of $FA_{1-x}Cs_xPbI_3$ perovskite between photoactive phase (α phase) and non-photoactive phase (δ phase) under humidity, as well as the reversible healing of degraded devices, is monitored. Moreover, through in situ atomic force microscopy, the kinetic transition between α and δ phase is revealed to be the "nucleation–growth transition" process. Density functional theory calcula-tion implies an enthalpy-driven α-to-δ degradation process during humidity aging and an entropy-driven δ-to-α healing process at high temperatures. The α phase of $FA_{1-x}Cs_xPbI_3$ can be stabilized at elevated temperature under high humidity due to the increased nucleation barrier, and the resulting non-encap-sulated PSCs retain >90% of their initial efficiency after >1000 h at 60 °C and 60% relative humidity. This finding provides a deepened understanding on the phase-transition process of $FA_{1-x}Cs_xPbI_3$ from both thermodynamics and kinetics points of view, which also presents an effective means to stabilize the α phase of FA-dominated perovskites and devices for practical applications.

1. Introduction

Organic–inorganic hybrid halide perovskite solar cells (PSCs) have obtained rapid development due to their excellent opto-electronic properties[1–6] and low fabrication cost, wherein their power conversion efficiency (PCE) has rapidly improved up to 25.7% within 13 years.[7] This type of perovskites is generally

in the form of ABX_3, in which the A-site cations are usually composed of $CH_3NH_3^+$ (MA^+), $CH(NH_2)_2^+$ (FA^+), and mono-valent metal cations (such as Cs^+), the B-site cations are Pb^{2+} or Sn^{2+}, and the X-site anions are halogen ions. Recently, mixed A-site cation perovskite based on FA^+ and Cs^+ ($FA_{1-x}Cs_xPbI_3$) becomes pop-ular because of its desired optoelectronic properties and good thermal stability.[8–15] In addition, compared with pure $FAPbI_3$ with a tolerance factor slightly greater than 1[16] and prone to phase transition into non-photoactive phase (δ phase) at room temperature,[17–19] $FA_{1-x}Cs_xPbI_3$ shows better phase stability, in which photoactive α phase is thermodynamically stable at room temperature.[16,20–22] The improved phase stability of $FA_{1-x}Cs_xPbI_3$ is stemmed from: 1) the similar crystal structure and volume per stoichiometric unit between α-$FAPbI_3$ and α-$CsPbI_3$, which results in the small internal energy input during the formation of the mixed system α-$FA_{1-x}Cs_xPbI_3$; 2) the slightly increased internal energy and greatly increased mixing entropy lead to a totally reduced free energy for α-$FA_{1-x}Cs_xPbI_3$ system.[22–24]

However, as a mixed system with ionic nature, $FA_{1-x}Cs_xPbI_3$ still suffers from phase instability under operational conditions, e.g., light, heat, electrical field, and humidity.[21,25–27] The phase instability issues of $FA_{1-x}Cs_xPbI_3$ include phase separation and

H. Liu, N. Li, F. Wang, Y. Zhang, Z. Huang, H. Zhou
Beijing Key Laboratory for Theory and Technology of Advanced Battery Materials
Key Laboratory of Polymer Chemistry and Physics of Ministry of Education
School of Materials Science and Engineering
Peking University
Beijing 100871, P. R. China
E-mail: happy_zhou@pku.edu.cn
Z. Chen, S. Tao
Materials Simulation and Modelling
Department of Applied Physics
Eindhoven University of Technology
Eindhoven 5600 MB, The Netherlands

Z. Chen, S. Tao
Center for Computational Energy Research
Department of Applied Physics
Eindhoven University of Technology
P.O. Box 513, Eindhoven 5600 MB, The Netherlands
C. Li, L. Jiang
Institute of Chemistry
Chinese Academy of Sciences
Beijing 100190, China
X. Niu, Q. Chen, T. Song
School of Materials Science and Engineering
Beijing Institute of Technology
Beijing 100081, P. R. China

phase transition. Researchers first noticed its phase separation phenomenon and the underlying mechanism has been recently explored. Schelhas et al. observed the evolution of structural stability in mixed A-site perovskites during device operation by the in situ X-ray diffraction measurement, and pointed out that the degradation pathway of $FA_{1-x}Cs_xPbI_3$ perovskite was related to the phase separation into the binary phase.[21] Subsequently, Li et al. characterized the light aged $FA_{1-x}Cs_xPbI_3$ perovskite through photoluminescence and synchrotron-based X-ray fluorescence microscopy, identified the heterogeneous distribution of Cs and FA in nanoscale. First principle density functional theory (DFT) calculations revealed that the injection of photogenerated carriers into FA-rich regions under illumination became the thermodynamic driving force for phase separation.[27] Despite the progress on the understanding of phase separation within $FA_{1-x}Cs_xPbI_3$, the phase transition accompanied with phase separation cannot be ignored. Previous work indicated that the phase separation and phase transition were coexisted in $FA_{1-x}Cs_xPbI_3$ under high humidity, with degraded species of δ-$FAPbI_3$ and δ-$CsPbI_3$.[28] With respect to α-to-δ phase-transition process of $FAPbI_3$, researchers have observed thermal hysteresis of the phase transition between α phase and δ phase due to the potential barrier between them,[29] as well as the formation of δ phase started at the grain boundary (upon moisture invasion) and then proceeded toward the interior of the grains.[30] However, the thermodynamic origin and kinetic process of the corresponding phase transition in FA-based perovskites, especially $FA_{1-x}Cs_xPbI_3$ are still unclear. Thus, it is essential to understand the phase-transition process of $FA_{1-x}Cs_xPbI_3$ and explore the full picture of its degradation mechanism, which can guide the effective strategies to improve the intrinsic phase stability of the FA-dominated perovskites.

Herein, we first monitored the reversible phase-transition process of $FA_{1-x}Cs_xPbI_3$ perovskite, namely α-to-δ phase (humidity aging) and δ-to-α phase (heat healing). The film properties and the corresponding device performance during this reversible phase-transition process were systematically investigated. The degraded devices were found to be healed after heating treatment. Through in-situ atomic force microscopy (AFM) characterization, the phase transition between α and δ phase could be revealed as "nucleation–growth transition" process. DFT calculations revealed that the thermodynamic driving force for α-to-δ transition under high humidity was the configurational enthalpy, while the δ-to-α transition was dominated by the vibrational entropy under high temperature. Finally, the α-phase $FA_{1-x}Cs_xPbI_3$ could be stabilized under high humidity at elevated temperature ($\approx$60 °C) due to the increased δ-phase nucleation barrier associated with the entropy change. The resulting nonencapsulated PSCs retained over 90% of their initial efficiency after aging at 60 °C and 60% relative humidity (RH) stressors for 1000 h. Our research provides a clear picture of phase-transition kinetics and thermodynamics of $FA_{1-x}Cs_xPbI_3$, which aids the development of effective means to stabilize the photoactive phase of perovskite for practical application.

2. Results and Discussion

A reversible phase transition of $FA_{0.9}Cs_{0.1}PbI_3$ was clearly observed under humidity and heating condition (**Figure 1**a), respectively. That is, the freshly fabricated perovskite (Initial sample) changed from black to yellow (Aged sample) after 2 days storage at 60% RH and room temperature ($\approx$25 °C) under dark, and the Aged sample could recover to black after heating at 150 °C in air ($\approx$60% RH) under dark for several minutes (Healed sample, Figure S1, Supporting Information). We then systematically investigated the phase states and optoelectronic properties of relevant perovskites under this phase-transition process. For Initial sample, the X-ray diffraction (XRD) patterns
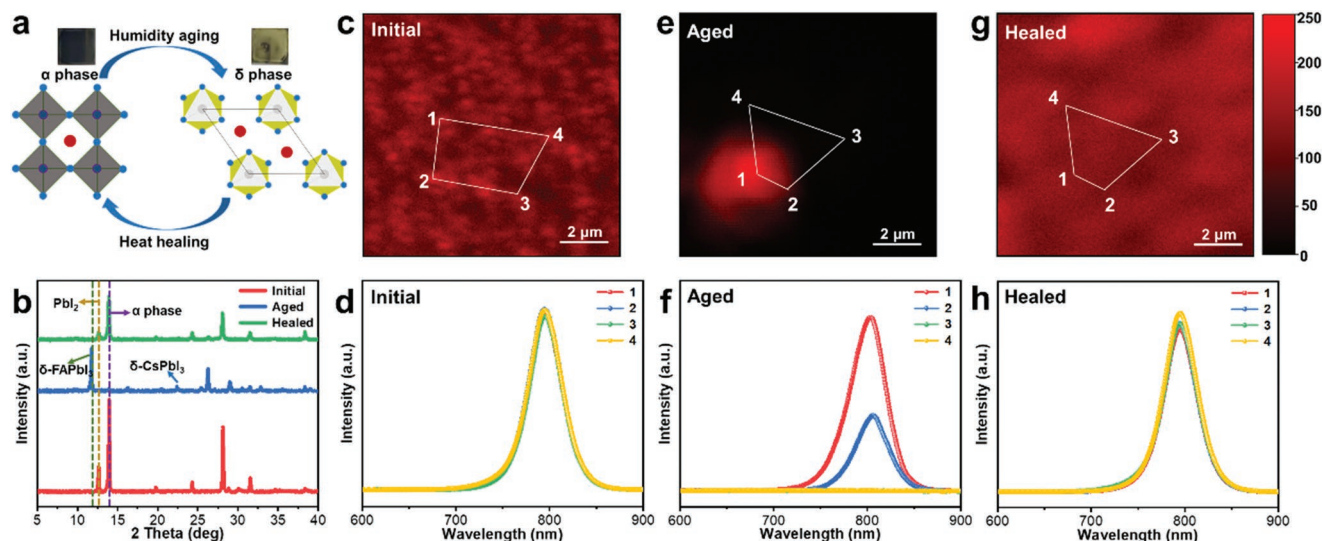
Figure 1. Reversible phase transition of $FA_{0.9}Cs_{0.1}PbI_3$. a) Schematic diagram of reversible phase transition in FA-dominated perovskite. b) XRD patterns of the Initial sample, Aged sample, and Healed sample. c,e,g) The PL mapping images of the Initial sample (c), Aged sample (e), and Healed sample (g). d,f,h) The corresponding PL spectra of the selected positions in the Initial sample (d), Aged sample (f), and Healed sample (h). (c,e) were collected from the same sample but not the same area through ex situ observations due to a long-time ($\approx$2 days) α-to-δ degradation process. (e,g) were collected in the same area through in situ observations.

(Figure 1b) proved that the perovskite was mainly composed by α phase with the strong diffraction peak at 14.0°, corresponding to the (001) plane of the cubic structure.[20] This was also evidenced by UV–vis absorption measurement (Figure S2, Supporting Information), where the absorption of sample was similar with α-phase $FA_{0.9}Cs_{0.1}PbI_3$ perovskite with the bandgap at about 1.54 eV.[20] To characterize the spatial uniformity of the Initial sample, we collected the photoluminescence (PL) mapping images (Figure 1c and Figure S3 (Supporting Information)). The overall PL intensity of the Initial sample was relatively uniform (Figure S4, Supporting Information). We then selected several positions in the image (marked as 1–4 in Figure 1c) and obtained the corresponding PL emission spectra (Figure 1d). The emission peaks in these positions were all located at about 796 nm, which proved that the perovskite was mainly composed by α-phase $FA_{0.9}Cs_{0.1}PbI_3$.[31] In addition, they all exhibited single emission peak with narrow full width at half maximum (FWHM, ≈40 nm), indicating that there were no phase separation in the Initial sample.

The existence of humidity would trigger an obvious phase transition of perovskite, as evidenced by XRD patterns (Figure 1b). The Aged sample was mainly composed by the δ-phase $FAPbI_3$ (the diffraction peak at 11.8°, corresponding to the (010) plane[32]) and δ-phase $CsPbI_3$ (the diffraction peak at 22.7°, corresponding to the (112) plane[33]), while the diffraction peaks of the α phase were almost disappeared. The UV–vis absorption of Aged sample was also similar with the δ-phase $FAPbI_3$ with ≈2.5 eV bandgap (Figure S2, Supporting Information).[34] Then, we selected several positions in the PL mapping image of Aged sample (Figure 1e, the location of these positions were different from Figure 1c (ex situ testing process)) and obtained the corresponding PL emission spectra (Figure 1f). Particularly, only few regions in PL mapping image (positions 1–2) exhibited the similar PL emission with Initial sample (Figure 1e), the PL intensities of most regions in the Aged sample were substantially weak (Figure S4, Supporting Information). The α phase emission peak at about 796 nm was also hardly detected at positions 3–4 (Figure 1f). This result further indicated that the overwhelming phase in Aged sample was photo-inactive δ phase. Combined with above characterizations, we speculated that most regions in Aged sample have experienced the α-to-δ phase-transition process.

However, the δ-phase perovskite could transform back to the α phase when the Aged sample was heated at 150 °C for 3 min. As shown in Figure 1b, the diffraction peak of α-phase (14.0°, 24.2°, 28.0°, 31.5° for (001), (111), (002), (012) planes, respectively) reappeared in the Healed sample, without any signal for δ-phase perovskites. In addition, we observed that the PbI_2 peak in Initial sample disappeared after humidity aging, then reappeared after heat healing (Figure 1b), which was discussed in Figure S5 (Supporting Information). The UV–vis spectrum (Figure S2, Supporting Information) also proved the existence of the α phase, indicating that the δ-to-α phase transition occurred. Moreover, we characterized the spatial phase distribution of Healed sample through the in situ PL mapping measurements: Compared to Aged sample before heating (Figure 1e and Figure S4 (Supporting Information)), the overall PL intensity was substantially enhanced after heat healing (Figure 1g and Figure S4 (Supporting Information)). We selected the

same positions (positions 1–4 in Aged sample) to check the corresponding spectra, where the PL emission peaks in Healed sample were all located at 796 nm with narrow FWHM (41 nm, Figure 1h), indicating that the Healed sample was mainly composed of the photoactive α phase. These phenomena further confirmed that the phase state and relevant optical properties of FA-dominated perovskites could be reversibly transformed.

To examine whether the reversible phase transition could lead to the recovery of device performance, we then fabricated n–i–p-structured PSCs (indium tin oxide (ITO)/ SnO_2/$FA_{0.9}Cs_{0.1}PbI_3$/hole-transport layer (HTL)/Au) to conduct the "humidity aging–heat healing" cycles. The statistics of photovoltaic parameters for freshly fabricated PSCs with 2,2″,7,7″-tetrakis[N,N-di(4-methoxyphenyl)amino]-9,9′-spirobifluorene (spiro-OMeTAD) as the HTL (Figure S6, Supporting Information) showed an average PCE of 22.0 ± 0.7%, while the champion device achieved a PCE of 22.70% (which reached the high level PCE in $FA_{0.9}Cs_{0.1}PbI_3$ devices[35]) based on the high quality perovskite films (Figure S7 and Table S1, Supporting Information). We finally chose poly[bis(4-phenyl) (2,4,6-trimethylphenyl)amine] (PTAA)-based devices to perform the "humidity aging–heat healing" cycles to avoid severe degradation of HTL at high temperature (≈150 °C).[36] More details regarding the device architecture and the fabrication procedure were described in the Supporting Information. The freshly fabricated device exhibited the PCE of 18.05% with the V_{OC} of 1.037 V, short-circuit current (J_{SC}) of 23.60 mA cm^{-2}, fill factor (FF) of 73.75%. During the humidity aging (≈60% RH), the PCE of the device gradually decreased to nearly zero after 6 days (**Figure 2**d), wherein the major loss was the J_{SC} (Figure 2b). We attributed it to the perovskite phase transition from α (photoactive) to δ (photo-inactive) under humidity, and the δ phase could not contribute to the photocurrent under illumination due to the increased bandgap and reduced light absorption ability (Figure S2, Supporting Information). While, the reductions of V_{OC} and FF during humidity aging were not obvious (Figure 2a,c), mainly due to the devices still retaining a small amount of residual α phase after humidity aging (Figure 1e and **Figure 3**a). Then, we heated the aged devices at 150 °C for 3 min for healing, the perovskite underwent δ-to-α phase transition and the PCE of the corresponding device recovered to 18.64% (with the V_{OC} of 1.032 V, J_{SC} of 23.34 mA cm^{-2}, FF of 77.42%). This value was even slightly higher than that of the initial PSC, which likely stemmed from the better contact between adjacent layers in the device. Therefore, we argued that the performance of δ-phase $FA_{0.9}Cs_{0.1}PbI_3$-based devices could be healed under simple heating. Moreover, we repeated the "humidity aging–heat healing" cycles for 3 times in the same sample, the device performance could still maintain the similar level with that of the initial state (Figure 2a–e and Table S2 (Supporting Information)). This suggested that the facile heat healing process may serve as an alternative means to prolong the lifetime of FA-based PSCs.

To reveal the kinetics within the phase transition, we thoroughly investigate the healing process from δ to α phase. The in situ optical microscope was first applied to examine the phase-transition pathways upon heating. As shown in Figure 3a, white regions in Aged sample were speculated to be δ phase due to its large bandgap (which allowed most visible
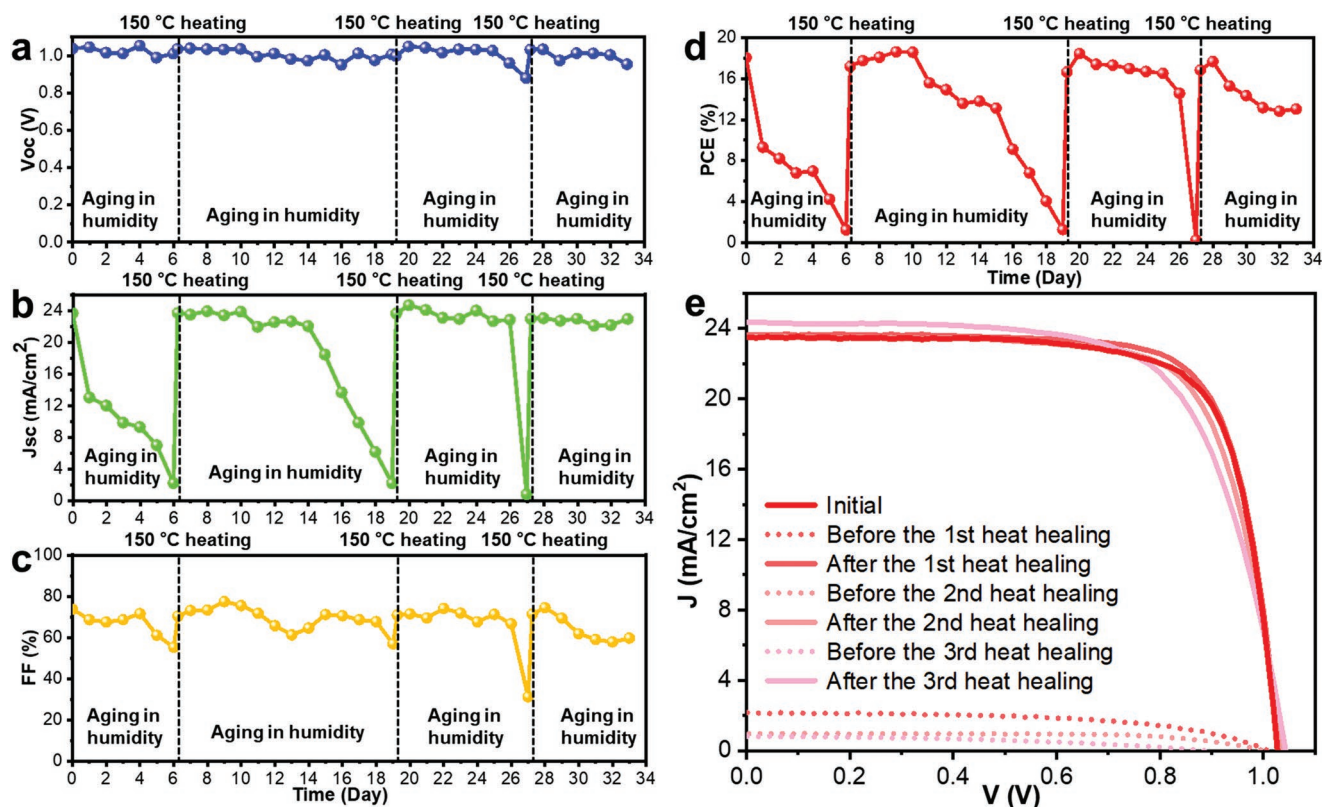
Figure 2. Performance healing of the aged devices by heating treatment. a–d) Changes of V_{OC} (a), J_{SC} (b), FF (c), and PCE (d) of same device during three cycles of "humidity aging–heat healing." e) J–V curves of the device during the "humidity aging–heat healing" cycles.

light transmission), while black regions were α phase due to its capability of absorbing visible light. The white regions were dominated in the Aged sample, with quite few black regions, which was consistent with the PL mapping image in Figure 1e. The sample was then heated with gradually elevated temperature, and there was no obvious change below 130 °C. When the temperature reached 140 °C, black regions began to expand with white regions shrinking, indicating the occurrence of δ-to-α phase transition. The film was further heated at 150 °C to accelerate the phase- transition process, and the black regions became dominant after 3 min, suggesting that the δ phase was basically transformed into α phase. It should be noted that the δ-to-α phase transition was initiated at multiple sites and in particular, preferentially expanded along with the existing α-phase seeds (Figure 3a), which was similar to the nucleation and growth of crystals in the traditional crystallization process.

The ex situ XRD (Figure 3b) and PL measurements (Figure S8, Supporting Information) were simultaneously performed to confirm the phase state during the heat healing process. For the Aged samples before heating, the film was mainly composed of δ phase (Figure 3b) with the weak PL emission at 796 nm (Figure S8, Supporting Information, corresponding to a small amount of α-phase emission). During the heat healing process (150 °C heating), the intensity of the δ-phase diffraction peak (11.8°) gradually diminished after 3 min (Figure 3b), indicating the substantially reduced content of δ phase in the film. Meanwhile, the intensity of the α-phase diffraction peak (14.0°) appeared and gradually increased under heating, meaning the

successful δ-to-α phase transition. Similarly, the PL emission of the Aged sample at 796 nm gradually increased during the heat healing process, finally close to the Initial sample (Figure S9, Supporting Information). Moreover, the ex situ UV–vis spectra (Figure S10, Supporting Information) also proved the successive δ-to-α phase transition under heating, which could be completed within 3 min.

The in situ AFM measurement was then conducted to monitor the microscopic changes of perovskite morphology during the heat healing process (Figure 3c and Figure S11 (Supporting Information)). As shown in Figure 3c, the selected region (red dotted line marked) in the Aged sample exhibited a large grain (≈3 μm) with smooth surface, which was consistent with the scanning electron microscopy (SEM) results (Figure S12, Supporting Information). This sample was then heated at 150 °C, wherein some smaller grains gradually appeared within the large grain with clear grain boundaries (GBs). Combined with XRD patterns (Figure 3b), we speculated that the δ-phase large grains were separated into several α-phase small grains. This was also supported by SEM images (Figure S12, Supporting Information), wherein the grain size of the Aged sample was ≈4 μm, while the grain size of the Healed sample was only ≈500 nm (similar with Initial sample of ≈400 nm). Considering the grain size variation between α-phase (small) and δ-phase (large) perovskites, the morphology elevation indicated that the α-to-δ phase transition was occurred by the coalescence of several α-phase grains under the humidity, while the δ-to-α phase transition was

**ADVANCED
SCIENCE NEWS**

www.advancedsciencenews.com
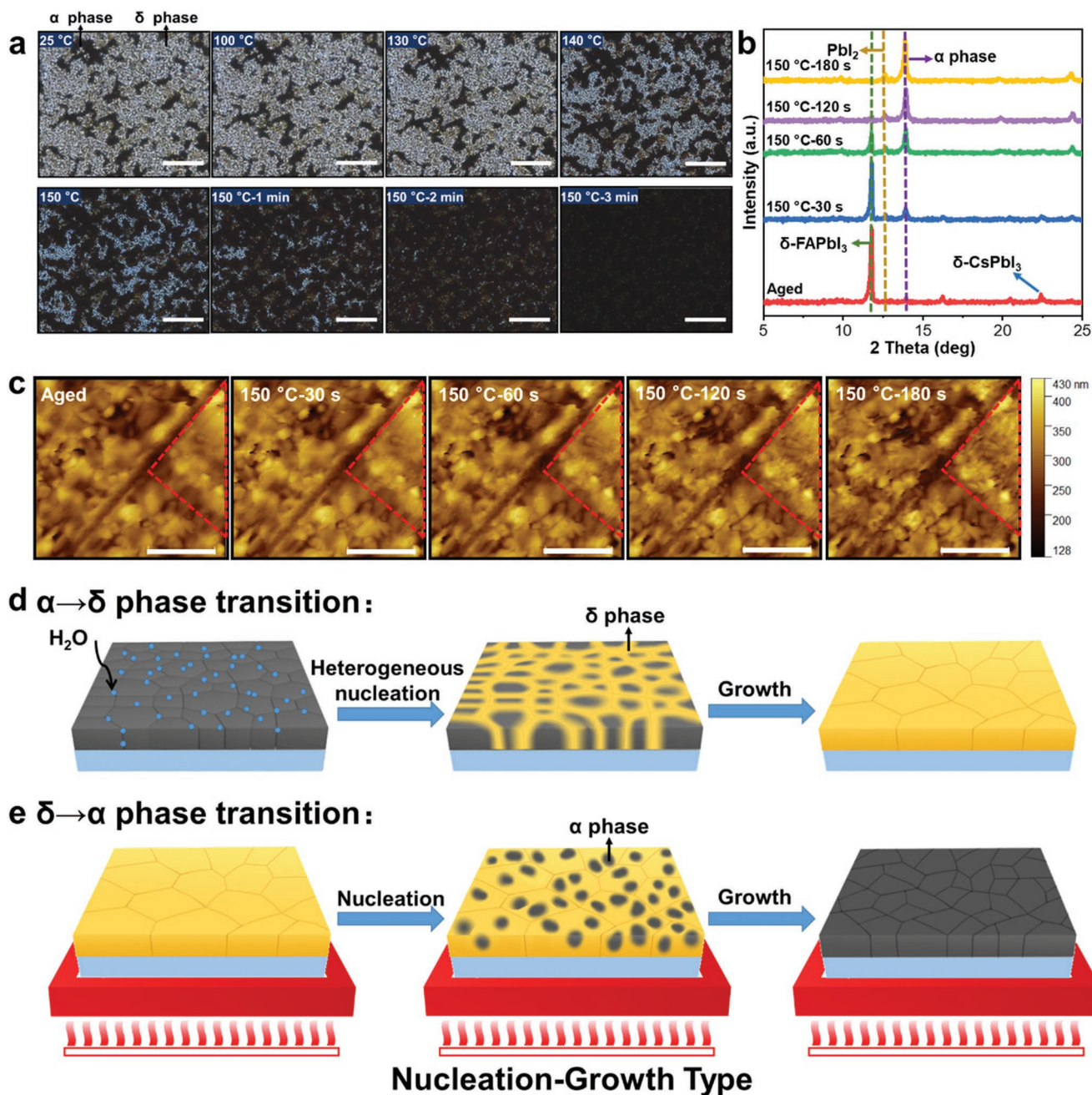
**ADVANCED
MATERIALS**

www.advmat.de

Figure 3. Microscopic changes in perovskite films during heat healing. a) In situ optical microscopy images of the Aged sample during heat healing. Scale bar: 5 μm. b) XRD patterns of the Aged sample at different stages of heat healing. c) In situ AFM topography images of the perovskite films during heat healing. Scale bar: 2 μm. d,e) Schematic diagram of phase-transition microprocess.

achieved by a superposition of nucleation events for individual crystallites within δ-phase grains.

Combining the above results, we speculated that the kinetic process during perovskite phase transition was "nucleation–growth" type. As shown in Figure 3d, for α-phase perovskites, the existence of GBs provided the sites for ion migration and then local structure reconstruction through the uncoordinated ions and vacancies. Therefore, under humidity aging, the H_2O could react with perovskite and preferentially induced defect generation[37] and lattice distortion at GBs to initiate the total

phase transition. In addition, the defects (such as vacancies) at GBs could release the lattice strain to accommodate the shape and volume changes during phase transition, thus the nuclei could easily form along the GBs with reduced free-energy barrier, especially under the H_2O invasion. Once the heterogeneous nucleation of δ phase occurred, the α-to-δ phase transition would continuously conduct under humidity. Eventually these δ-phase nuclei could grow into large grains, similar to the coalescence of closely packed α-phase grains shown in AFM[30] and SEM images (Figure S12, Supporting Information). For

δ-phase perovskites (Figure 3e), under the heating process, high temperature could provide sufficient driving force for δ-to-α phase transition, resulting in small nucleation barrier and small critical nucleation radius for the α phase. In addition, the effect of heat on the atomic structure of materials was accelerating the vibration of atoms, and higher temperature would lead to more intense atom vibration. Therefore, fluctuation of energy, structure, and composition would significantly occur in δ-phase grains at high temperature, leading to a higher probability to form the α-phase nuclei with critical size. Hence, plenty of α-phase nuclei would form inside the δ-phase large grains in a short time, which have been proved by in situ AFM characterizations (Figure 3c and Figure S11 (Supporting Information)). Continuous heating would then accelerate the growth of α-phase nuclei until the δ-phase perovskite was completely transformed into α phase.

The thermodynamic origin of such phase transition (α-to-δ under high humidity and δ-to-α under high temperature) was also studied. **Figure 4**a illustrated the moisture-induced degradation process of α-FA$_{0.9}$Cs$_{0.1}$PbI$_3$ at low temperatures. The composition in FA$_{0.9}$Cs$_{0.1}$PbI$_3$ was normally fluctuated, which led to the spontaneous occurrence of α-FAPbI$_3$ and α-CsPbI$_3$ domains at the grain surfaces or GBs. It was known that both α-FAPbI$_3$ and α-CsPbI$_3$ were readily phase transformed to δ phases at room temperature when exposed to moisture.[30,38] The moisture catalyzed the α-to-δ phase
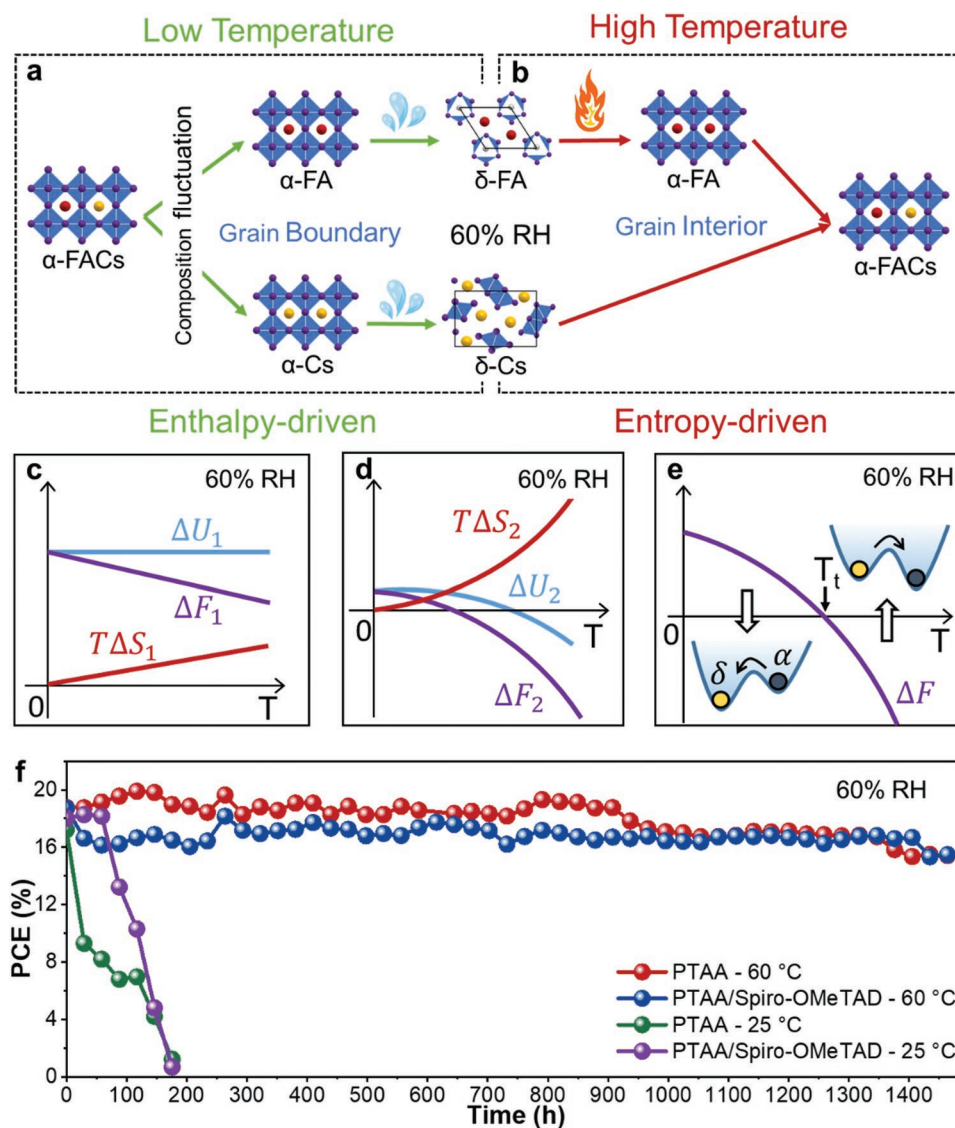

Figure 4. Mechanism of the reversible phase transition and the related device stability. a,b) Schematics of the enthalpy-driven degradation process at low temperatures (a) and the entropy-driven healing process at high temperatures (b). c) Relative configurational free energy (ΔF_1), d) vibrational free energy (ΔF_2), and e) total free energy ($\Delta F = \Delta F_1 + \Delta F_2$) as a function of temperature T that accounts for the reversible (α-FA$_{0.9}$Cs$_{0.1}$PbI$_3 \leftrightarrow \delta$FAPbI$_3 + \delta$CsPbI$_3$) phase transition between α phase and δ phase, with a transition temperature at T_t. Here ΔU_1, ΔU_2, ΔS_1, and ΔS_2 denote the relative value of configurational enthalpy, vibrational enthalpy, configurational entropy, and vibrational entropy of α phase with respect to the δ phase, respectively. f) Storage stability performance of PTAA-, PTAA/spiro-OMeTAD-based devices without encapsulation under 60 °C and 60% RH conditions or 25 °C and 60% RH conditions.

ADVANCED
SCIENCE NEWS

www.advancedsciencenews.com

ADVANCED
MATERIALS

www.advmat.de

transition by reducing the free energy barrier such that it accelerates the ion migration near the GBs where the formation of the δ phase commences.[30,37] DFT calculations showed that the relative configurational enthalpy ΔU_1 of α-FA$_{0.9}$Cs$_{0.1}$PbI$_3$ could be reduced by 53 meV [formula unit (f.u.)]$^{-1}$ due to the α-to-δ(α-FA$_{0.9}$Cs$_{0.1}$PbI$_3 \rightarrow \delta$-FAPbI$_3 + \delta$-CsPbI$_3$) phase transition, where $\Delta U_1 = E(\alpha$-FA$_{1-x}$Cs$_x$PbI$_3) - (1-x)E(\delta$-FAPbI$_3) - xE(\delta$-CsPbI$_3)$. Here, $x = 1/9$ was used for the computations and $E(\alpha$-FA$_{1-x}$Cs$_x$PbI$_3)$, $E(\delta$-FAPbI$_3)$, $E(\delta$-CsPbI$_3)$ stood for the DFT calculated total energies of the three compounds, respectively (see the Supporting Information for computational details). The relative configurational entropic contribution ($T\Delta S_1$) was about 9 meV f.u.$^{-1}$ at room temperature, failing to fully compensate the enthalpic contribution ΔU_1. This yielded a positive relative configurational free energy ($\Delta F_1 = \Delta U_1 - T\Delta S_1$) of about 44 meV f.u.$^{-1}$ at room temperature, as illustrated in Figure 4c.

Figure 4b depicted the healing process at high temperatures, where the reversed δ-to-α (δ-FAPbI$_3$ + δ-CsPbI$_3 \rightarrow \alpha$-FA$_{0.9}$Cs$_{0.1}$PbI$_3$) phase transition occurred when the temperature was increased to $T_t \approx 140$ °C (Figure 3a). Here, the δ-to-α transition temperature T_t of FA$_{0.9}$Cs$_{0.1}$PbI$_3$ was close to that of pure FAPbI$_3$ ($T_t \approx 165$ °C),[16] but much lower than that of pure CsPbI$_3$ ($T_t \approx 315$ °C),[16] suggesting that the δ-to-α healing process in this work might start with a δ-to-α phase transition of pure δ-FAPbI$_3$ to α-FAPbI$_3$ phase inside the grains. As the Cs cations were mobile at high temperatures, the α-FAPbI$_3$ could be stabilized by the partial replacement of FA cations by Cs,[27] consequently leading to the formation of energetically favored α-FA$_{0.9}$Cs$_{0.1}$PbI$_3$ with uniform element distribution. This was also evidenced by time-of-flight secondary ion mass spectrometry (TOF-SIMS, Figures S13–S15, Supporting Information): the initial perovskite film exhibited uniform Cs distribution, which generated some Cs-rich regions after humidity aging, and then recovered to relatively uniform Cs distribution after heating. If the polymorphous nature of perovskites for the cubic phase had been considered,[39] the temperature-dependent δ-to-α phase transition for FAPbI$_3$ could be computationally predicted at about 157 °C,[40] which was close to the experimentally observed transition temperature.[16] On the other hand, the relative configurational entropic contribution of α phase with respective to δ phase, $T\Delta S_1$, at 140 °C was about 12 meV f.u.$^{-1}$, playing a minor role in δ-to-α transition. In that sense, we should consider the vibrational contribution to the free energy which was normally insignificant at low temperatures but significant at high temperatures.[40] The relative vibrational free energy of α phase with respective to δ phase was given by $\Delta F_2 = \Delta U_2 - T\Delta S_2$, where ΔU_2 was the vibrational enthalpy difference of α phase and δ phase and ΔS_2 was the vibrational entropy difference of α phase and δ phase (Figure 4d). It was predicted to be the relative vibrational entropic contribution, $T\Delta S_2$, in analogy to the phase transition in pure δ-FAPbI$_3$, that mainly and fully compensated the α-to-δ enthalpic difference (ΔU_1) when $T > T_t$, thus provided the driving force for δ-to-α phase transition (where the $\Delta F = \Delta F_1 + \Delta F_2 < 0$ was expected, Figure 4e).

Moreover, according to nucleation theory, there was a barrier for α-to-δ phase transition under high humidity, as shown in Figure 4e. Therefore, the resultant α-phase FA$_{0.9}$Cs$_{0.1}$PbI$_3$ might be kinetically stabilized at elevated temperature under high

humidity by increasing the $T(\Delta S_1 + \Delta S_2)$ to decrease ΔF, thus raising the α-to-δ transition barrier ($\Delta F^* \propto 1/(\Delta F)^2$). This was evidenced by our experimental results: there was no detectable δ phase when the freshly fabricated α-FA$_{0.9}$Cs$_{0.1}$PbI$_3$ was heated at 60 °C under 60% RH, no matter under dark (Figure S16, Supporting Information) or illumination (Figure S17, Supporting Information). Moreover, the corresponding PSC device (with different type HTLs) without encapsulation could maintain over 90% of its initial PCE after storing at 60 °C and 60% RH conditions for 1000 h, while the PCE of the same device dropped to nearly 0 within 150 h at 25 °C and 60% RH conditions (Figure 4f). This result further confirmed that the moderate temperature was beneficial for the phase stability of FA$_{1-x}$Cs$_x$PbI$_3$ perovskites under humidity. The use of 60 °C has proven to be effective to stabilize α phase, which was also close to the operation temperature of solar cells.[41]

3. Conclusions

We have conducted an in-depth study on the phase-transition kinetics and thermodynamics of FA-dominated perovskites. For the first time, we experimentally proved a reversible phase-transition process of FA$_{1-x}$Cs$_x$PbI$_3$ perovskite between α phase and δ phase under humidity, as well as the reversible healing of the degraded film and devices. Based on an in situ AFM characterization, we revealed a "nucleation–growth transition" between α and δ phase. Theoretical analysis implied an enthalpy-driven α-to-δ degradation process during humidity aging and an entropy-driven δ-to-α healing process at high temperatures. The resultant α phase FA$_{0.9}$Cs$_{0.1}$PbI$_3$ was kinetically stabilized at elevated temperature under high humidity by increasing the entropy to enhance the α-to-δ transition barrier, and the relevant nonencapsulated devices could retain over 90% of its initial efficiency after storing at 60 °C and 60% RH conditions for 1000 h. Our finding deepened the understanding of the intrinsic phase stability of FA$_{1-x}$Cs$_x$PbI$_3$, presented an effective method to stabilize the α phase FA$_{1-x}$Cs$_x$PbI$_3$ under high humidity, eventually improved the phase stability of FA$_{1-x}$Cs$_x$PbI$_3$ photovoltaics.

4. Experimental Section

Materials and Reagents: SnO$_2$ colloid precursor (tin(IV) oxide, 15% in H$_2$O colloidal dispersion) was purchased from Alfa Aesar. PbI$_2$ (99.999%), CsI (99.9%), *N,N*-dimethylformamide (DMF, 99.9%), dimethyl sulfoxide (DMSO, 99.5%), isopropanol (99.5%), and chlorobenzene (99.9%) were purchased from Sigma-Aldrich. Spiro-OMeTAD (99.8%) and PTAA (MOS) were purchased from Xi'an Polymer Light Technology in China. ITO substrate was purchased from Advanced Election Technology Co., Ltd.

Material Synthesis: FAX (FAI and FACl) were synthesized using the methods reported previously.[42] The details including 8.8 g formamidine acetate ethanol solution (0.1 mol) were added into a 100 mL three neck flask that was immersed in a water-ice bath. A certain amount (0.12 mol) of HX acid was slowly dropped into the bottle with continuous stirring. The mixture was refluxed for 2 h under N$_2$ atmosphere. Subsequently, the solution was concentrated to a dry solid by using rotary evaporation at 90 °C. This crude product was redissolved into 20 mL ethanol, then 100 mL diethyl ether was slowly dropped along the bottle wall, and a white product would deposit. This recrystallization was repeated 3 times, and the obtained precipitation was dried in a vacuum oven for 24 h at

40 °C. The final products were sealed in a N_2-filled glove box for future use.

Solar Cell Fabrications: The ITO substrate was cleaned with ultrapure water, acetone, ethanol, and isopropanol, successively. After 30 min of UV–O_3 treatments, a SnO_2 nanocrystal solution (2.5%, diluted by water) was spin coated onto the substrate at 4000 rpm for 30 s and then annealed at 150 °C for 30 min in air. The perovskite film was fabricated by a two-step solution process: the PbI_2 (1.3 M, dissolved in DMF:DMSO [9:1, v/v]) mixed with 10% CsI was spin coated onto ITO/SnO_2 at 2300 rpm for 30 s and annealed at 70 °C for 1 min in a nitrogen glove box. After cooling the PbI_2-coated substrate to room temperature in a nitrogen glove box, a mixed organic cation solution (FAI 0.35 M; FACl 0.07 M, dissolved in isopropanol) was spin coated with 2000 rpm for 30 s and then annealed at 150 °C for 30 min in air. Then, the spiro-OMeTAD/PTAA HTL solution, in which a spiro-OMeTAD/PTAA (36/5 mg mL^{-1}, dissolved in chlorobenzene) mixed solution was employed with the addition of 35 μL bis (trifluoromethane) sulfonimide lithium salt (Li-TFSI) (260 mg mL^{-1}, dissolved in acetonitrile), and 30 μL 4-*tert*-butylpyridine (*t*BP) was deposited by spin coating at 3000 rpm for 30 s. In case of PTAA HTL solution (15 mg mL^{-1}, dissolved in chlorobenzene), 7.5 μL of Li-TFSI (260 mg mL^{-1}, dissolved in acetonitrile) and 7.5 μL of *t*BP were added. In case of spiro-OMeTAD HTL solution (75 mg mL^{-1}, dissolved in chlorobenzene), 35 μL of Li-TFSI (260 mg mL^{-1}, dissolved in acetonitrile) and 30 μL of *t*BP were added. The device was finished by thermal evaporation of Au (100 nm) under vacuum.

Basic Material Characterization: The morphology of perovskite thin films was measured using a cold field-emission SEM equipment (Hitachi S-4800). The XRD patterns were collected using a PANalytical X'Pert Pro X-ray powder diffractometer with Cu Kα radiation (λ = 1.54050 Å). Steady-state PL was measured by FLS980 (Edinburgh Instruments Ltd.) in air (temperature was about 25 °C, humidity was about 30% RH) with the excitation wavelength at 470 nm, and the emission signal was collected in the wavelength range from 600 to 900 nm. The UV–vis absorption spectra were obtained by an UV–visible diffuse reflectance spectrophotometer (Japan Hitachi UH4150). The *J*–*V* characteristics of perovskite devices were obtained using a Keithley 2400 source-measure unit under AM1.5G illumination at 1000 W m^{-2} with a Newport Thermal Oriel 91192 1000 W solar simulator.

PL Mapping Characterization: PL mapping was measured by a laser scanning confocal microscope (Enlitech, SPCM-1000) equipped with a 470 nm pulse laser and galvo-based scanner in air (temperature at about 18 °C, humidity at about 10% RH). The excitation wavelength was also 470 nm, and the emission signal was collected in the wavelength range from 375 to 1025 nm. The signal collection area for each sample was 512 × 512 and 1024 × 1024. The PL images in Figure 1c,g were not collected in the same area as α-to-δ process took a relatively long time (≈2 days) during humidity aging, but in Figure 1e,g were collected in the same area through in situ observations due to the fast transition of δ-to-α process.

In Situ AFM Characterization: All the AFM characterizations were carried out using an AFM microscope (Cypher ES, Oxford Instruments) in air with a polyheater and an environmental controller to achieve the required temperature and deliver local photoelectric properties of the sample at variable temperatures in situ.

Density Functional Theory Calculation: To calculate the total energy of α-FA$_{0.9}$Cs$_{0.1}$PbI$_3$, start was from a periodic supercell of the α-FAPbI$_3$ containing 27 formula units, with a 3 × 3 × 3 expansion of (pseudo) cubic perovskite building block. Three FA cations were then replaced by Cs at different lattice positions. Three possible configurations were considered. To calculate the total energies of hexagonal δ-FAPbI$_3$ and orthorhombic δ-CsPbI$_3$, a 2 × 2 × 3 supercell (24 formula units) and a 2 × 4 × 1 supercell (32 formula units), respectively, were taken.

The total energy calculations were performed using the DFT approach. The mixed Gaussian and plane-wave method[43] (QUICKSTEP formalism) and the Perdew–Burke–Ernzerhof exchange-correlation functional within the generalized gradient approximation[44], as implemented in the CP2K code, were used.[45] The van der Waals interactions through the DFT-D3

scheme[46] were included to account for dispersion interactions and to obtain optimal lattice constants. The Gaussian basis set employed for all atoms was a double-ζ polarized basis set with polarization functions[47] in conjunction with the Goedecker–Teter–Hutter pseudopotentials.[48] The plane-wave cutoff for the expansion of the electron density was set to 450 Ry (6123 eV). The shape and volume of the supercell, as well as the atomic positions were fully optimized. The convergence criteria on forces were set at 4.5×10^{-4} Har Bohr^{-1} (0.02 eV Å^{-1}).

The relative configurational enthalpy of α-FA$_{0.9}$Cs$_{0.1}$PbI$_3$, with respect to δ-FAPbI$_3$ and δ-CsPbI$_3$, could be calculated by

$$\Delta U_1 = E(\alpha - FA_{1-x}Cs_xPbI_3) - (1-x)E(\delta - FAPbI_3) - xE(\delta - CsPbI_3) \tag{1}$$

where $E(...)$ were the calculated DFT total energies per formula unit of α-FA$_{0.9}$Cs$_{0.1}$PbI$_3$, δ-FAPbI$_3$, and δ-CsPbI$_3$, respectively. $x = 1/9$ was used for all calculations in this work. The average value of the total energies of the three inequivalent configurations for α-FA$_{0.9}$Cs$_{0.1}$PbI$_3$ was taken. Taking the entropy (ΔS_1) into account allowed for computing the relative configurational free energy per f.u. $\Delta F_1 = \Delta U_1 - T\Delta S_1$, where T is the temperature. The relative configurational entropy was approximated as

$$\Delta S_1 = -k_B \left[x \ln x + (1-x) \ln(1-x) \right] \tag{2}$$

where k_B is the Boltzmann constant. It was noted that the vibrational free energy normally played a dominant role in phase transition at high temperatures due to the strong vibration of soft modes in perovskites.[40] The relative vibrational free energy of α phase with respective to δ phase was given by $\Delta F_2 = \Delta U_2 - T\Delta S_2$, where ΔU_2 is the vibrational enthalpy difference of α phase and δ phase, and ΔS_2 is the vibrational entropy difference of α phase and δ phase. To sum up, the relative total free energy of α phase with respective to δ phase should be considered as $\Delta F = \Delta U_1 + \Delta U_2 - T(\Delta S_1 + \Delta S_2)$. Since the δ-to-α phase-transition temperature of CsPbI$_3$ was substantially higher than 140 °C as mentioned in main text and the δ-CsPbI$_3$ was not the major component of yellow phase, it was expected that the δ-to-α phase transition in "δ-FAPbI$_3$ + δ-CsPbI$_3$" should be sensibly similar to the δ-to-α phase transition in δ-FAPbI$_3$, where the vibrational entropy played the central role at high temperatures.[40]

Statistical Analysis: All statistics analyses were performed with Origin 2022. The data obtained from XRD (Figures 1b and 3b), PL mapping, in situ PL mapping, PL, *J*–*V*, in situ optical microscope, in situ AFM, UV–vis, SEM, TOF-SIMS were the original data without normalization. The data of the XRD patterns (Figures S16a and S17a, Supporting Information) were normalized. The statistical distribution data of PCE, J_{SC}, V_{OC}, and FF (Figure S6, Supporting Information) were got from 20 independent devices.

Supporting Information

Supporting Information is available from the Wiley Online Library or from the author.

Acknowledgements

Conflict of Interest

The authors declare no conflict of interest.

Data Availability Statement

Research data are not shared.

Keywords

[1] W.-J. Yin, T. Shi, Y. Yan, *Adv. Mater.* **2014**, *26*, 4653.

[2] Y. Ogomi, A. Morita, S. Tsukamoto, T. Saitho, N. Fujikawa, Q. Shen, T. Toyoda, K. Yoshino, S. S. Pandey, T. Ma, S. Hayase, *J. Phys. Chem. Lett.* **2014**, *5*, 1004.

[3] S. D. Stranks, G. E. Eperon, G. Grancini, C. Menelaou, M. J. P. Alcocer, T. Leijtens, L. M. Herz, A. Petrozza, H. J. Snaith, *Science* **2013**, *342*, 341.

[4] G. Xing, N. Mathews, S. Sun, S. S. Lim, Y. M. Lam, M. Grätzel, S. Mhaisalkar, T. C. Sum, *Science* **2013**, *342*, 344.

[5] C. S. Ponseca, T. J. Savenije, M. Abdellah, K. Zheng, A. Yartsev, T. Pascher, T. Harlang, P. Chabera, T. Pullerits, A. Stepanov, J.-P. Wolf, V. Sundström, *J. Am. Chem. Soc.* **2014**, *136*, 5189.

[6] N. Li, X. Niu, L. Li, H. Wang, Z. Huang, Y. Zhang, Y. Chen, X. Zhang, C. Zhu, H. Zai, S. Ma, H. Liu, X. Liu, Z. Guo, G. Liu, R. Fan, H. Chen, J. Wang, Y. Lun, X. Wang, J. Hong, H. Xie, D. S. Jakob, X. G. Xu, Q. Chen, H. Zhou, *Science* **2021**, *373*, 561.

[7] NREL Best Research-Cell Efficiency Chart, https://www.nrel.gov/pv/cell-efficiency.html (accessed: August 2022).

[8] N. Zhou, Y. Shen, Y. Zhang, Z. Xu, G. Zheng, L. Li, Q. Chen, H. Zhou, *Small* **2017**, *13*, 1700484.

[9] S.-H. Turren-Cruz, A. Hagfeldt, M. Saliba, *Science* **2018**, *362*, 449.

[10] Y. Chen, Z. Yang, X. Jia, Y. Wu, N. Yuan, J. Ding, W.-H. Zhang, S. Liu, *Nano Energy* **2019**, *61*, 148.

[11] Y. Deng, S. Xu, S. Chen, X. Xiao, J. Zhao, J. Huang, *Nat. Energy* **2021**, *6*, 633.

[12] Z. Wang, D. P. McMeekin, N. Sakai, S. van Reenen, K. Wojciechowski, J. B. Patel, M. B. Johnston, H. J. Snaith, *Adv. Mater.* **2017**, *29*, 1604186.

[13] Z. Yang, W. Zhang, S. Wu, H. Zhu, Z. Liu, Z. Liu, Z. Jiang, R. Chen, J. Zhou, Q. Lu, Z. Xiao, L. Shi, H. Chen, L. K. Ono, S. Zhang, Y. Zhang, Y. Qi, L. Han, W. Chen, *Sci. Adv.* **2021**, *7*, eabg3749.

[14] R. Chen, Y. Wu, Y. Wang, R. Xu, R. He, Y. Fan, X. Huang, J. Yin, B. Wu, J. Li, N. Zheng, *Adv. Funct. Mater.* **2021**, *31*, 2008760.

[15] J. Li, H. Wang, X. Y. Chin, H. A. Dewi, K. Vergeer, T. W. Goh, J. W. M. Lim, J. H. Lew, K. P. Loh, C. Soci, T. C. Sum, H. J. Bolink, N. Mathews, S. Mhaisalkar, A. Bruno, *Joule* **2020**, *4*, 1035.

[16] Z. Li, M. Yang, J.-S. Park, S.-H. Wei, J. J. Berry, K. Zhu, *Chem. Mater.* **2016**, *28*, 284.

[17] Q. Han, S.-H. Bae, P. Sun, Y.-T. Hsieh, Y. Yang, Y. S. Rim, H. Zhao, Q. Chen, W. Shi, G. Li, Y. Yang, *Adv. Mater.* **2016**, *28*, 2253.

[18] N. J. Jeon, J. H. Noh, W. S. Yang, Y. C. Kim, S. Ryu, J. Seo, S. I. Seok, *Nature* **2015**, *517*, 476.

[19] H. Liu, H. Zhou, *Chem. Res. Chin. Univ.* **2021**, *37*, 1055.

[20] J.-W. Lee, D.-H. Kim, H.-S. Kim, S.-W. Seo, S. M. Cho, N.-G. Park, *Adv. Energy Mater.* **2015**, *5*, 1501310.

[21] L. T. Schelhas, Z. Li, J. A. Christians, A. Goyal, P. Kairys, S. P. Harvey, D. H. Kim, K. H. Stone, J. M. Luther, K. Zhu, V. Stevanovic, J. J. Berry, *Energy Environ. Sci.* **2019**, *12*, 1341.

[22] C. Yi, J. Luo, S. Meloni, A. Boziki, N. Ashari-Astani, C. Grätzel, S. M. Zakeeruddin, U. Röthlisberger, M. Grätzel, *Energy Environ. Sci.* **2016**, *9*, 656.

[23] C. C. Stoumpos, C. D. Malliakas, M. G. Kanatzidis, *Inorg. Chem.* **2013**, *52*, 9019.

[24] D. M. Trots, S. V. Myagkota, *J. Phys. Chem. Solids* **2008**, *69*, 2520.

[25] I. L. Braly, R. J. Stoddard, A. Rajagopal, A. R. Uhl, J. K. Katahara, A. K. Y. Jen, H. W. Hillhouse, *ACS Energy Lett.* **2017**, *2*, 1841.

[26] C. M. Sutter-Fella, Q. P. Ngo, N. Cefarin, K. L. Gardner, N. Tamura, C. V. Stan, W. S. Drisdell, A. Javey, F. M. Toma, I. D. Sharp, *Nano Lett.* **2018**, *18*, 3473.

[27] N. Li, Y. Luo, Z. Chen, X. Niu, X. Zhang, J. Lu, R. Kumar, J. Jiang, H. Liu, X. Guo, B. Lai, G. Brocks, Q. Chen, S. Tao, D. P. Fenning, H. Zhou, *Joule* **2020**, *4*, 1743.

[28] K. Ho, M. Wei, E. H. Sargent, G. C. Walker, *ACS Energy Lett.* **2021**, *6*, 934.

[29] T. Chen, B. J. Foley, C. Park, C. M. Brown, L. W. Harriger, J. Lee, J. Ruff, M. Yoon, J. J. Choi, S.-H. Lee, *Sci. Adv.* **2016**, *2*, e1601650.

[30] J. S. Yun, J. Kim, T. Young, R. J. Patterson, D. Kim, J. Seidel, S. Lim, M. A. Green, S. Huang, A. Ho-Baillie, *Adv. Funct. Mater.* **2018**, *28*, 1705363.

[31] Y. Yu, C. Wang, C. R. Grice, N. Shrestha, J. Chen, D. Zhao, W. Liao, A. J. Cimaroli, P. J. Roland, R. J. Ellingson, Y. Yan, *ChemSusChem* **2016**, *9*, 3288.

[32] F. Ma, J. Li, W. Li, N. Lin, L. Wang, J. Qiao, *Chem. Sci.* **2017**, *8*, 800.

[33] Y. Hu, F. Bai, X. Liu, Q. Ji, X. Miao, T. Qiu, S. Zhang, *ACS Energy Lett.* **2017**, *2*, 2219.

[34] Y. H. Park, I. Jeong, S. Bae, H. J. Son, P. Lee, J. Lee, C.-H. Lee, M. J. Ko, *Adv. Funct. Mater.* **2017**, *27*, 1605988.

[35] L. Yang, J. Feng, Z. Liu, Y. Duan, S. Zhan, S. Yang, K. He, Y. Li, Y. Zhou, N. Yuan, J. Ding, S. Liu, *Adv. Mater.* **2022**, *34*, 2201681.

[36] F. M. Rombach, S. A. Haque, T. J. Macdonald, *Energy Environ. Sci.* **2021**, *14*, 5161.

[37] J. Lin, M. Lai, L. Dou, C. S. Kley, H. Chen, F. Peng, J. Sun, D. Lu, S. A. Hawks, C. Xie, F. Cui, A. P. Alivisatos, D. T. Limmer, P. Yang, *Nat. Mater.* **2018**, *17*, 261.

[38] R. J. Sutton, M. R. Filip, A. A. Haghighirad, N. Sakai, B. Wenger, F. Giustino, H. J. Snaith, *ACS Energy Lett.* **2018**, *3*, 1787.

[39] X.-G. Zhao, G. M. Dalpian, Z. Wang, A. Zunger, *Phys. Rev. B* **2020**, *101*, 155137.

[40] J. Yin, G. Teobaldi, L. M. Liu, *J. Phys. Chem. Lett.* **2022**, *13*, 3089.

[41] P. Holzhey, M. Saliba, *J. Mater. Chem. A* **2018**, *6*, 21794.

[42] N. Li, S. Tao, Y. Chen, X. Niu, C. K. Onwudinanti, C. Hu, Z. Qiu, Z. Xu, G. Zheng, L. Wang, Y. Zhang, L. Li, H. Liu, Y. Lun, J. Hong, X. Wang, Y. Liu, H. Xie, Y. Gao, Y. Bai, S. Yang, G. Brocks, Q. Chen, H. Zhou, *Nat. Energy* **2019**, *4*, 408.

[43] J. VandeVondele, M. Krack, F. Mohamed, M. Parrinello, T. Chassaing, J. Hutter, *Comput. Phys. Commun.* **2005**, *167*, 103.

[44] J. P. Perdew, K. Burke, M. Ernzerhof, *Phys. Rev. Lett.* **1996**, *77*, 3865.

[45] J. Hutter, M. Iannuzzi, F. Schiffmann, J. VandeVondele, *WIREs Comput. Mol. Sci.* **2014**, *4*, 15.

[46] S. Grimme, J. Antony, S. Ehrlich, H. Krieg, *J. Chem. Phys.* **2010**, *132*, 154104.

[47] J. VandeVondele, J. Hutter, *J. Chem. Phys.* **2007**, *127*, 114105.

[48] S. Goedecker, M. Teter, J. Hutter, *Phys. Rev. B* **1996**, *54*, 1703.